Method of Range Ambiguity Suppression Combining Sparse Reconstruction and Matched Filter

Meng Qi, Lijia Huang, Xiaochen Wang, Jie Li, and Bingchen Zhang

***Abstract*—Synthetic aperture radar (SAR) images are often affected by range ambiguity due to antenna sidelobe characteristics and pulse operating mechanism. The work of range ambiguity suppression focuses on both SAR system design and signal processing. On the one hand, ideas have been proposed to modify the transmitting and receiving waveforms to block the ambiguous energy, such as up and down chirp modulation, multiple elevation beams, and azimuth phase coding techniques. On the other hand, signal processing methods in echo and image domains have been used to reduce the range ambiguity energy, such as up and down chirp processing and sparse regularization methods. This article proposes a range ambiguity suppression method that combines sparse reconstruction and matched filter. There are four main steps: performing the sparse reconstruction to obtain the ambiguity area, estimating the ambiguity signal using the ambiguity area image and reconstruction matrix, separating the ambiguity signal from the whole signal to obtain the signal of the primary imaging area, and using the matched filter to the primary signal to obtain the main lobe area image. In this method, sparse reconstruction improves the accuracy of ambiguity signal estimation, and the matched filter ensures the efficiency of the imaging processing procedure. Simulation results show that the proposed method can effectively suppress range ambiguity. When the ambiguity energy is relatively strong, the focal underdetermined system solver algorithm can get better results than the classical orthogonal matching pursuit algorithm. Moreover, the weak targets and the details of the main lobe image are well preserved.**

***Index Terms*—Matched filter, range ambiguity suppression, SAR imaging, SAR system, sparse reconstruction.**

Manuscript received 30 July 2022; revised 6 September 2022; accepted 20 September 2022. Date of publication 30 September 2022; date of current version 11 October 2022. This work was supported in part by Youth Innovation Promotion Association under Grant 2019127 and in part by the Chinese Academy of Sciences. *(Corresponding author: Lijia Huang.)*

Meng Qi is with the Aerospace Information Research Institute, Chinese Academy of Sciences, Beijing 100094, China, also with the Key Laboratory of Technology in Geo-spatial Information Processing and Application System, Chinese Academy of Sciences, Beijing 100190, China, and also with the Aerospace Information Research Institute of QiLu, Chinese Academy of Sciences, Jinan 250100, China (e-mail: qimeng@aircas.ac.cn).

Lijia Huang, Xiaochen Wang, and Bingchen Zhang are with the Aerospace Information Research Institute, Chinese Academy of Sciences, Beijing 100094, China, and also with the Key Laboratory of Technology in Geo-spatial Information Processing and Application System, Chinese Academy of Sciences, Beijing 100190, China (e-mail: iecas8huanglijia@163.com; wangxc@radi.ac.cn; zhangbc@aircas.ac.cn).

Jie Li is with the Aerospace Information Research Institute, Chinese Academy of Sciences, Beijing 100094, China, also with the Key Laboratory of Technology in Geo-spatial Information Processing and Application System, Chinese Academy of Sciences, Beijing 100190, China, and also with the School of Electronic, Electrical and Communication Engineering, University of Chinese Academy of Sciences, Beijing 101408, China (e-mail: lijie195@mails.ucas.ac.cn).

Digital Object Identifier 10.1109/JSTARS.2022.3210907

I. Introduction

SYNTHETIC aperture radar (SAR) is an all-day, all-weather microwave remote sensing imaging radar with a wide range of applications. When the radar receives useful echoes from the antenna main lobe, the interference echoes from the antenna sidelobe are received at the same time. After the imaging process of these echoes, the range ambiguity problem arises, which makes false targets, and thus affects the SAR image quality. In recent years, the requirements for SAR image quality in radar remote sensing applications have gradually increased, such as resolution, swath width, NE σ^0, geolocation accuracy, radiation accuracy, range ambiguity to signal ratio, azimuth ambiguity to signal ratio, and so on [1]. At the same time, the increase of the radar resolution and the increase of the swath width aggravate the range ambiguity [2], so SAR range ambiguity suppression is an important task to improve SAR image quality.

At present, there are two main kinds of methods to solve the SAR range ambiguity problem. The first category is to reduce the reception of range ambiguity energy from the perspective of radar system design, such as elevation null spacing [3], azimuth phase coding [4], and up and down chirp modulating techniques [5]. With the exception of the technique of up and down chirp modulation, other techniques have not yet been adopted by launched spaceborne SAR systems. Another category of range ambiguity suppression aimed at the interference echoes that have already been received from the perspective of signal processing methods, including up and down chirp processing method applicable to up and down chirp modulation system [6], [7], and sparse regularization method applicable to single modulation system [8].

Using the technique of up and down chirp modulation [5], the radar transmits a positive frequency modulation signal and negative frequency modulation signal alternately, thus the echo from the first ambiguity area and the echo from the main lobe area have opposite frequency modulation slopes. The main lobe imaging processor will cause the ambiguity area to be defocused, thereby achieving range ambiguity suppression of peak intensity to some extent. In [6], Wen et al. proposed a new range ambiguity suppression method for the technique of up and down chirp modulation. By ignoring the range variance and establishing the matched filter of the first range ambiguity area, the superimposed image composed of the focused range ambiguity area image and the defocused main lobe area image is obtained. Next, a constant false alarm rate (CFAR) is used to detect the strong scattering points of the ambiguity area, and then the echo of the ambiguity

area can be estimated by the inverse matched filter, so as to realize the separation of the echoes of range ambiguity area and of the main lobe area.

Since 2006, the theory of compressive sensing proposed by Donoho [9] has developed rapidly, providing a theoretical basis for sparse microwave imaging. Peng et al. [10] proposed an optimization method for azimuth sampling parameters to improve the quality of sparsely reconstructed images. Fang et al. [11] established an observation matrix containing ambiguity image parameters and applied sparse reconstruction to range ambiguity suppression. Tian et al. [12] and Bi et al. [13] verified the performance and characteristics of the sparse reconstruction algorithm using a large amount of actual spaceborne SAR data. The sparse reconstruction algorithm has good range ambiguity suppression and noise suppression capabilities. Regularization-based sparse reconstruction is usually a biased estimation of the observed scene. Although it can obtain higher resolution images, it will cause a certain degree of radiation distortion, especially to weak targets, and cannot keep the statistical characteristics of the image as the classical matched filter algorithm can [14]. As a nonlinear algorithm, sparse reconstruction is much more computationally intensive than the classical matched filter algorithm, and its computational load increases sharply with the increase of scene size. In practical applications, various strategies are usually needed to accelerate the sparse reconstruction algorithm [15].

The sparse reconstruction algorithm has the capability of undersampled data processing. In the case of full sampling, a unified observation matrix can be constructed for the main lobe and sidelobe observation areas, so as to achieve the reconstruction and separation of both the main image and the range ambiguity image, and then the purpose of range ambiguity suppression is achieved. However, its computational complexity has a square relationship with the size of the observation matrix and also increases greatly with the size of the observation scene. The observation capability of spaceborne SAR, such as signal bandwidth, synthetic aperture time, and swath width, is getting higher and higher, so the scale of its observation matrix will become very large, and the sparse reconstruction algorithm is difficult to support the practical application of spaceborne SAR range ambiguity suppression.

The classical matched filter algorithm can set the matched filter parameters according to the range ambiguity area and obtain the focused range ambiguity image. At this time, the main image in the form of defocus is superimposed with the ambiguity area image, and the strong targets in the ambiguity area can be separated by CFAR detection [15]. The classical matched filter has good adaptability to the up and down chirp modulation system because the main image and the ambiguity image have opposite frequency modulation slopes, where the ambiguity image is focused and the main image is seriously defocused. However, for the fixed frequency modulation system, the main image is partly focused. The main image with stronger energy brings difficulties to CFAR detection, and thus it is difficult to effectively separate ambiguity image from the main image.

In this article, a range ambiguity suppression method combining matched filter and sparse reconstruction is proposed, that is, the ambiguity area is first reconstructed sparsely, the ambiguity area signal is estimated by using the image of the ambiguity area and the reconstruction matrix, and the ambiguity area can be separated from the whole signal. Then, the signal of the main image is obtained, and the main image is obtained by using matched filter algorithm. The method uses sparse reconstruction to improve the effectiveness of range ambiguity estimation and suppression and uses matched filter to improve the imaging processing efficiency and the ability to retain details of weak targets. The method has the range variance processing capability within the ambiguity image, compared with the article presented in [6] because the inverse procedure of sparse reconstruction reflects the range variance property. The method solves the range variance between the main image and the ambiguity image by two-step range migration correction and explains the applicable conditions of two different reconstruction algorithms.

TABLE I
VARIATION RANGE OF PIXEL ENERGY OF FOUR TYPICAL SCENES

Scenes	Max–Average (dB)	Max–Min (dB)
Mountainous Areas	15.93	68.32
Sea Surfaces	3.08	78.01
Ports	14.41	93.73
Urban Areas	17.74	96.06

The rest of this article is organized as follows. Section II introduces the sparse reconstruction method briefly and deduces the sparse reconstruction model for the range ambiguity area. The algorithm flow combining sparse reconstruction and matched filter is given. Section III provides the simulation experiment in detail, including the results and analysis of range ambiguity suppression of simulation point target, simulation surface target, and actual scene data. Finally, Section IV concludes this article.

II. RANGE AMBIGUITY SUPPRESSION METHOD

A. Principle of Combining Sparse Reconstruction and Matched Filter

The spaceborne SAR system adopts the pulse operating mechanism, and the actual illuminating area of the main lobe and sidelobe of the antenna on the ground is much larger than the observing area restricted by the radar receiving window. When the receiver receives the main lobe echo, it also receives the sidelobe echo of the preceding and subsequent pulses, forming a range ambiguity image and causing interference to the main image of the main lobe observation area.

For *X*-band, HH polarization, and submeter resolution images, based on the image data after processing and radiation correction (SLC data before quantify), Table I summarizes the relative pixel energy of four typical scenes: mountainous areas, sea surfaces (including islands and ships), ports, and urban areas. The pixel energy difference statistics includes the maximum to average range and the maximum to minimum range. It can be seen that the difference in pixel energy of these scenes can reach several tens of decibel. After the synthesized transmitting and receiving two-way patterns, the difference between the first sidelobe peak and the main lobe peak is about -20 dB, and the difference between the second sidelobe peak and the main lobe peak is

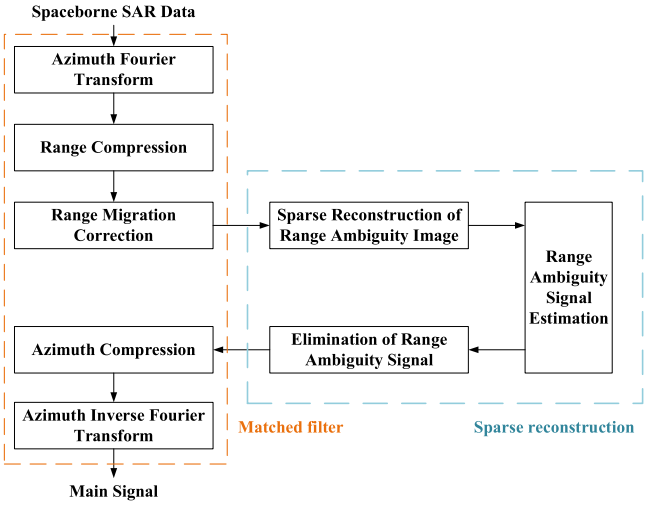

Fig. 1. Flowchart of range ambiguity suppression algorithm combining sparse reconstruction and matched filter.

about −40 dB or even lower, so the range ambiguity suppression is generally considered for the first sidelobe ambiguity area.

Fig. 1 shows the flowchart of our range ambiguity suppression algorithm. In the first step, we use matched filter to complete range compression and range migration correction, and then we use sparse reconstruction for the azimuth signal in each range gate to obtain the image of strong points of targets in the ambiguity area; next, we estimate the ambiguity signal by sparse reconstruction matrix and ambiguity image; finally, we use the matched filter for azimuth compression to obtain the main image after removing the ambiguity signal.

The total signal, which is composed of the main signal from the main lobe and the ambiguity signal from the sidelobe, can be expressed as

$$\boldsymbol{S}_E = \boldsymbol{S}_{\mathrm{MI}} + \boldsymbol{S}_{\mathrm{BI}} + N_{\mathrm{noise}} \tag{1}$$

where $\boldsymbol{S}_{\mathrm{MI}}$ represents the main signal, $\boldsymbol{S}_{\mathrm{BI}}$ represents the ambiguity signal, N_{noise} represents the noise signal, and $\boldsymbol{S}_E$ represents the total signal.

For meter-level resolution spaceborne SAR, the range migration difference between the main image and its ambiguity image is generally less than 0.5 times the resolution. For example, for *X*-band SAR satellites (such as TerraSAR-X), the finest resolution does not exceed 1 m; for *C*-band SAR satellites (such as Gaofen-3), the finest resolution does not exceed 1.8 m. After range compression and range migration correction, the main data and its ambiguity data can be expressed as one-dimensional azimuth signals in the Doppler domain whose expression is as follows:

$$s(f_\eta; R_c) = \sigma W_a(f_\eta) \times \exp\left[-j\frac{4\pi R_c}{\lambda}\sqrt{1-\left(\frac{\lambda f_{\mathrm{dc}}}{2V_r}\right)^2}\sqrt{1-\left(\frac{\lambda f_\eta}{2V_r}\right)^2}\right] \tag{2}$$

where f_η represents the azimuth frequency axis, R_c and f_{dc} represent the slant range and Doppler center frequency of the imaging center time (reference zero time), respectively, λ represents the radar wavelength, σ represents the radar backscattering cross section of target, $W_a(\cdot)$ represents the envelope of the azimuth signal in Doppler domain, and V_r represents the effective radar velocity.

In the main imaging area, the target vector formed by the target points in the same range gate can be expressed as

$$\mathrm{X}_{\mathrm{MI}} = \begin{pmatrix} \sigma_{1,\mathrm{MI}} & \sigma_{2,\mathrm{MI}} & \cdots & \sigma_{N,\mathrm{MI}} \end{pmatrix}^{\mathrm{T}} \tag{3}$$

where X_{MI} consists of N target points, $\sigma_{n,\mathrm{MI}}$ represents the radar backscattering cross section of the *n*th target point in X_{MI}, and T represents the vector transposition.

With respect to target vector X_{MI}, the target vectors of the first near and far ambiguity areas located in the same range gate as X_{MI} are given by $\mathrm{X}_{\mathrm{BI}=-1}$ and $\mathrm{X}_{\mathrm{BI}=+1}$, abbreviated as $\mathrm{X}_{\mathrm{BI}-}$ and $\mathrm{X}_{\mathrm{BI}+}$, respectively. $\mathrm{X}_{\mathrm{BI}-}$ and $\mathrm{X}_{\mathrm{BI}+}$ can be expressed as follows:

$$\mathrm{X}_{\mathrm{BI}-} = \begin{pmatrix} \sigma_{1,\mathrm{BI}-} & \sigma_{2,\mathrm{BI}-} & \cdots & \sigma_{N,\mathrm{BI}-} \end{pmatrix}^{\mathrm{T}} \tag{4}$$

$$\mathrm{X}_{\mathrm{BI}+} = \begin{pmatrix} \sigma_{1,\mathrm{BI}+} & \sigma_{2,\mathrm{BI}+} & \cdots & \sigma_{N,\mathrm{BI}+} \end{pmatrix}^{\mathrm{T}} \tag{5}$$

where $\mathrm{X}_{\mathrm{BI}-}$ and $\mathrm{X}_{\mathrm{BI}+}$ consist of N target points, and $\sigma_{n,\mathrm{BI}-}$ and $\sigma_{n,\mathrm{BI}+}$ represent the radar backscattering cross section of the *n*th target point in $\mathrm{X}_{\mathrm{BI}-}$ and $\mathrm{X}_{\mathrm{BI}+}$, respectively.

According to (2), the observation matrix $\boldsymbol{\Phi}_{\mathrm{MI}}$ is constructed for the target vector X_{MI}. $\boldsymbol{\Phi}_{\mathrm{MI}}$ is M rows multiplied by N columns, and the *m*th row and *n*th column element in $\boldsymbol{\Phi}_{\mathrm{MI}}$ can be expressed as

$$\varphi_{m,n,\mathrm{MI}} = \exp\left[-j\frac{4\pi R_c}{\lambda}\sqrt{1-\left(\frac{\lambda f_{\mathrm{dc}}}{2V_r}\right)^2}\sqrt{1-\left(\frac{\lambda f_{\eta|m}}{2V_r}\right)^2} - j2\pi f_{\eta|m}\eta_{c|n}\right] \tag{6}$$

where $f_{\eta|m}$ represents the *m*th sampling point of the azimuth frequency axis, $m = 1, 2, \ldots, M$; $\eta_{c|n}$ represents the beam center time of the *n*th target in the target vector X_{MI}, $n = 1, 2, \ldots, N$.

According to (6), the observation matrices $\boldsymbol{\Phi}_{\mathrm{BI}-}$ and $\boldsymbol{\Phi}_{\mathrm{BI}+}$ are, respectively, constructed for the target vectors $\mathrm{X}_{\mathrm{BI}-}$ and $\mathrm{X}_{\mathrm{BI}+}$. $\mathrm{X}_{\mathrm{BI}-}$ and $\mathrm{X}_{\mathrm{BI}+}$ have the same matrix size with X_{MI}, and the elements $\varphi_{m,n,\mathrm{BI}-}$ and $\varphi_{m,n,\mathrm{BI}+}$ in $\mathrm{X}_{\mathrm{BI}-}$ and $\mathrm{X}_{\mathrm{BI}+}$ are, respectively, expressed as

$$\varphi_{m,n,\mathrm{BI}-} = \exp\left[-j\frac{4\pi}{\lambda}\left(R_c - \frac{c}{2\mathrm{PRF}}\right)\sqrt{1-\left(\frac{\lambda f_{\mathrm{dc}}}{2V_r}\right)^2} \times\sqrt{1-\left(\frac{\lambda f_{\eta|m}}{2V_r}\right)^2} - j2\pi f_{\eta|m}\eta_{c|n}\right] \tag{7}$$

$$\varphi_{m,n,\mathrm{BI}+} = \exp\left[-j\frac{4\pi}{\lambda}\left(R_c + \frac{c}{2\mathrm{PRF}}\right)\sqrt{1-\left(\frac{\lambda f_{\mathrm{dc}}}{2V_r}\right)^2} \times\sqrt{1-\left(\frac{\lambda f_{\eta|m}}{2V_r}\right)^2} - j2\pi f_{\eta|m}\eta_{c|n}\right] \tag{8}$$

where PRF represents the pulse repetition frequency.

Therefore, the signal in (1) can be further expressed as

$$\boldsymbol{S}_E = \boldsymbol{\Phi}_{\mathrm{MI}}\mathrm{X}_{\mathrm{MI}} + \boldsymbol{\Phi}_{\mathrm{BI}-}\mathrm{X}_{\mathrm{BI}-} + \boldsymbol{\Phi}_{\mathrm{BI}+}\mathrm{X}_{\mathrm{BI}+} + N_{\mathrm{noise}}. \quad (9)$$

Associating the first three components, (9) can be rearranged as follows:

$$\boldsymbol{S}_E = \boldsymbol{\Phi}\mathrm{X} + N_{\mathrm{noise}} \quad (10)$$

where $\boldsymbol{\Phi}$ represents the whole observation matrix composed of the main imaging area observation matrix and the near and far ambiguity area observation matrices, and X represents the whole target vector composed of the main imaging area target points and the near and far ambiguity area target points

$$\boldsymbol{\Phi} = \left[\begin{array}{ccc} \boldsymbol{\Phi}_{\mathrm{BI}-} & \boldsymbol{\Phi}_{\mathrm{MI}} & \boldsymbol{\Phi}_{\mathrm{BI}+} \end{array}\right] \quad (11)$$

$$\mathrm{X} = \left[\begin{array}{ccc} \mathrm{X}_{\mathrm{BI}-} & \mathrm{X}_{\mathrm{MI}} & \mathrm{X}_{\mathrm{BI}+} \end{array}\right]^{\mathrm{T}}. \quad (12)$$

For the model shown in (10), in a condition that both the main imaging area and the ambiguity area have spatially sparse distribution property, the estimated value $\tilde{\mathrm{X}}$ of X is obtained by solving the minimum l_0 norm of X

$$\tilde{\mathrm{X}} = \arg\min_x \|\mathrm{X}\|_0, \quad \text{s.t. } \|\boldsymbol{\Phi}\mathrm{X} - \boldsymbol{S}_E\|_2 \le \varepsilon \quad (13)$$

where $\|\|_0$ and $\|\|_2$ represent the 0-norm and 2-norm of the orientation vector, respectively, and $\varepsilon \ge 0$, which is the parameter determined by the strength of the additive noise.

The ambiguity image reconstruction can be expressed as

$$\tilde{\mathrm{X}}_{\mathrm{BI}} = \left[\begin{array}{cc} \tilde{\mathrm{X}}_{\mathrm{BI}-} & \tilde{\mathrm{X}}_{\mathrm{BI}+} \end{array}\right]^{\mathrm{T}}. \quad (14)$$

The estimation result $\tilde{\boldsymbol{S}}_{\mathrm{BI}}$ of the ambiguity signal $\boldsymbol{S}_{\mathrm{BI}}$ based on the observation matrix and estimated ambiguity image can be expressed as

$$\tilde{\boldsymbol{S}}_{\mathrm{BI}} \approx \boldsymbol{\Phi}_{\mathrm{BI}}\tilde{\mathrm{X}}_{\mathrm{BI}}. \quad (15)$$

The ambiguity signal is subtracted from the acquired total signal, and the estimation result $\tilde{\boldsymbol{S}}_{\mathrm{MI}}$ of the main signal $\boldsymbol{S}_{\mathrm{MI}}$ is obtained by

$$\tilde{\boldsymbol{S}}_{\mathrm{MI}} = \boldsymbol{S}_E - \tilde{\boldsymbol{S}}_{\mathrm{BI}}. \quad (16)$$

Subsequent azimuth matched filter processing is performed on the signal $\tilde{\boldsymbol{S}}_{\mathrm{MI}}$, so as to achieve the range ambiguity suppression effect based on sparse reconstruction and matched filter. After azimuth matched filtering, the azimuth focused signal $s_{\mathrm{ac}}(\eta; R_c)$ is obtained by

$$s_{\mathrm{ac}}(\eta; R_c) = \mathrm{IFFT}\left\{\tilde{\boldsymbol{S}}_{\mathrm{MI}}(f_\eta; R_c) \cdot \exp\left(j\frac{4\pi R_c}{\lambda}\sqrt{1-\left(\frac{\lambda f_{\mathrm{dc}}}{2V_r}\right)^2}\sqrt{1-\left(\frac{\lambda f_\eta}{2V_r}\right)^2}\right)\right\}. \quad (17)$$

For the lower energy of the main imaging area, the range ambiguity problem is probably more obvious. If the main imaging area is distributed scene with relatively weaker energy, such as the sea surface and the desert, and the ambiguity image has spatially sparse distribution property, the above-mentioned ambiguity image sparse reconstruction process can be further simplified. In practical applications, all the images are often obtained by the matched filter for the first time. Then, for the images blurred by range ambiguity, the proposed method can be used to obtain high-quality images. Thereby, we can determine the type of main and ambiguous imaging areas.

In the simplified process, we no longer need to find the sparse solution of the observation matrix $\boldsymbol{\Phi}_{\mathrm{MI}}$ of the main imaging area and only need to find the sparse solution of the observation matrix $\boldsymbol{\Phi}_{\mathrm{BI}}$ in the ambiguity area. Accordingly, the total signal can be approximately expressed as

$$\boldsymbol{S}_E \approx \boldsymbol{\Phi}_{\mathrm{BI}}\mathrm{X}_{\mathrm{BI}} + N_{\mathrm{noise}} \quad (18)$$

where $\boldsymbol{\Phi}_{\mathrm{BI}}$ represents the whole ambiguity area observation matrix composed of $\boldsymbol{\Phi}_{\mathrm{BI}-}$ and $\boldsymbol{\Phi}_{\mathrm{BI}+}$, and X_{BI} represents the whole ambiguity area target vector composed of $\mathrm{X}_{\mathrm{BI}-}$ and $\mathrm{X}_{\mathrm{BI}+}$. The signal from the main imaging area equivalently becomes noise, which has a certain impact on the ambiguity image reconstruction accuracy

$$\boldsymbol{\Phi}_{\mathrm{BI}} = \left[\begin{array}{cc} \boldsymbol{\Phi}_{\mathrm{BI}-} & \boldsymbol{\Phi}_{\mathrm{BI}+} \end{array}\right] \quad (19)$$

$$\mathrm{X}_{\mathrm{BI}} = \left[\begin{array}{cc} \mathrm{X}_{\mathrm{BI}-} & \mathrm{X}_{\mathrm{BI}+} \end{array}\right]^{\mathrm{T}}. \quad (20)$$

Similarly to (13), the estimated value $\tilde{\mathrm{X}}_{\mathrm{BI}}$ of X_{BI} is obtained by solving the minimum l_0 norm of X_{BI}

$$\tilde{\mathrm{X}}_{\mathrm{BI}} = \arg\min_x \|\mathrm{X}_{\mathrm{BI}}\|_0, \quad \text{s.t.} \|\boldsymbol{\Phi}_{\mathrm{BI}}\mathrm{X}_{\mathrm{BI}} - \boldsymbol{S}_E\|_2 \le \varepsilon. \quad (21)$$

B. Improvements in Range Migration Correction

With the resolution improvement, the differential range migration between the main imaging area and the ambiguity area increases and even exceed one range gate. As mentioned above, if the range migration correction is designed for the main imaging area, the residual migration of the ambiguity area will affect the range ambiguity suppression effect of our algorithm.

In order to solve the problem of accurate reconstruction of ambiguity image in high-resolution case, the algorithm implement procedure, as shown in Fig. 1, is further improved. The range migration correction step is divided into two steps: the first step is carried out before the sparse reconstruction step, where the range migration of the ambiguity area is precisely corrected; the second step is carried out after the sparse reconstruction step, where the residual range migration of the main imaging area is precisely corrected. The improved algorithm flowchart is shown in Fig. 2. Although the improved algorithm has one more step and an amount of calculation is added, it can ensure the accuracy of the sparse reconstruction and matched filter, as well as the range ambiguity suppression effect of the proposed algorithm.

C. Comparison of Sparse Reconstruction Algorithms

Sparse reconstruction algorithm can solve the ill-posed problem of compressed sensing. In this article, we use the sparse reconstruction algorithm to build the relatively strong point targets in ambiguity area so that the requirements of the sparse reconstruction algorithm are not very high. Now, this article compares two classical algorithms: the orthogonal matching

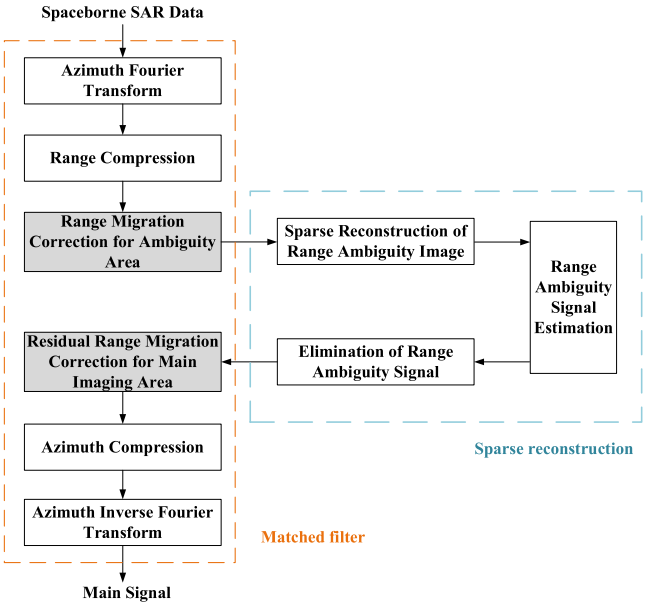

Fig. 2. Flowchart of range ambiguity suppression algorithm by improving range migration correction.

TABLE II
IMPLEMENTATION STEPS OF OMP ALGORITHM

Input: measurement matrix Θ, observation vector y, sparsity K;
Output: sparse approximation $\tilde{\alpha}^K$ of signal α to be solved;
Initialization: $\tilde{\alpha}^0 = 0$, $\Lambda^0 = \varnothing$;
Iteration step: $for \quad k = 0 \quad to \quad K-1$
$z^k = \Theta^H \ y - \Theta\tilde{\alpha}^k$
$\Lambda^{k+1} = \Lambda^k \cup \arg\min_i \left\|z_i^k\right\|$
$\tilde{\alpha}^{k+1} = \ \Theta_{\Lambda^{k+1}}^H \Theta_{\Lambda^{k+1}}^{\ \ -1} \Theta_{\Lambda^{k+1}}^H y$
end

pursuit (OMP) algorithm and the focal underdetermined system solver (FOCUSS) algorithm.

1) OMP Algorithm: OMP algorithm belongs to the greedy pursuit algorithm [16], which is a classical category of the sparse reconstruction algorithm. The solution can be achieved iteratively. In each iteration, a local optimal solution is given, and after several iterations, a globally optimal solution can be made. OMP algorithm is widely used because it is simple to implement. Most of the existing greedy pursuit algorithms are developed on the basis of OMP, such as regularized OMP [17]. The implementation steps of a representative OMP algorithm are given in Table II.

The OMP algorithm essentially selects the column in the measurement matrix that has the greatest contribution to the signal energy. When the sparsity is small, the signal can be quickly reconstructed, but when the sparsity is large, the reconstruction speed is slow and the accuracy is limited. In OMP algorithm, the sparsity needs to be presented, and if inappropriate, the reconstruction accuracy will deteriorate.

TABLE III
IMPLEMENTATION STEPS OF FOCUSS ALGORITHM

Input: measurement matrix Θ, observation vector y, regularization parameter λ, gradient descent parameter μ;
Output: sparse approximation $\tilde{x}^{k_{\max}+1}$ of signal x to be solved;
Initialization: $\tilde{x}^0 = 0$;
Iteration step: $for \quad k = 0 \quad to \quad k_{\max}$
$z^{k+1} = \tilde{x}^k - \mu\Theta^H \ \Theta\tilde{x}^k - y$
$x^{k+1} = \mathrm{H}_{\lambda\mu,p} \ z_{\ +1}$
end

2) FOCUSS Algorithm: FOCUSS algorithm belongs to nonconvex optimization algorithm [18], which converts the difficult l_0 norm solving problem into a resolvable l_p norm. At present, the research articles of $l_{1/2}$ regularization and $l_{2/3}$ regularization are relatively mature. The solution of $l_{1/2}$ regularization can be obtained by the gradient descent method. The implementation steps of the FOCUSS algorithm are given in Table III.

The FOCUSS algorithm is essentially an improved least square method based on iterative weighting, which uses *a posteriori* knowledge for iterative weighting to approximate the real sparse solution. The reconstruction accuracy is usually higher than that of OMP algorithm. If the regularization parameter and the gradient descent parameter are not suitable, the FOCUSS algorithm may converge to a local minimum in the iteration and resulting in invalid reconstruction.

The computational complexity of the algorithm in this article is approximately $1/P$ of the traditional sparse reconstruction algorithm, where P is the proportion of the reconstructed scene size to the total scene size and is determined by the satellite parameters and the radar parameters.

III. EXPERIMENTAL RESULTS AND ANALYSIS

In this section, the experiments are divided into two parts. In the first part, we use point target and surface target simulation to verify the proposed method quantitatively and to compare the accuracy and applicability of the OMP and the FOCUSS algorithms. In the second part, we use the actual image as simulating scene to verify the visual effect of our method.

A. Simulation of Point Target and Surface Target

The simulation parameters are given in Table IV.

The simulation is carried out for the point target. The doppler centroid frequency of the main and ambiguous targets is equal, and the center time slant range of them differs about c/(2PRF). In the first case, the energy ratio of the ambiguous target to the main target is 1:1 (ambiguous target energy minus main target energy in dB is 0 dB). The energy refers to the reached energy of the radar receiver modulated by a two-way antenna pattern. Fig. 3 shows the imaging results obtained by matched filter, by our

TABLE IV
SIMULATION PARAMETERS

Parameters	Value	Unit
Carrier Frequency	9.6	GHz
Radar Bandwidth	100	MHz
Pulse Repetition Frequency	5000	Hz
Slant Range of Center Time	600	km
Satellite Velocity	7000	m/s
Synthetic Aperture Time	0.7	s
Nominal Range Resolution	<2.0	m
Nominal Azimuth Resolution	<2.0	m

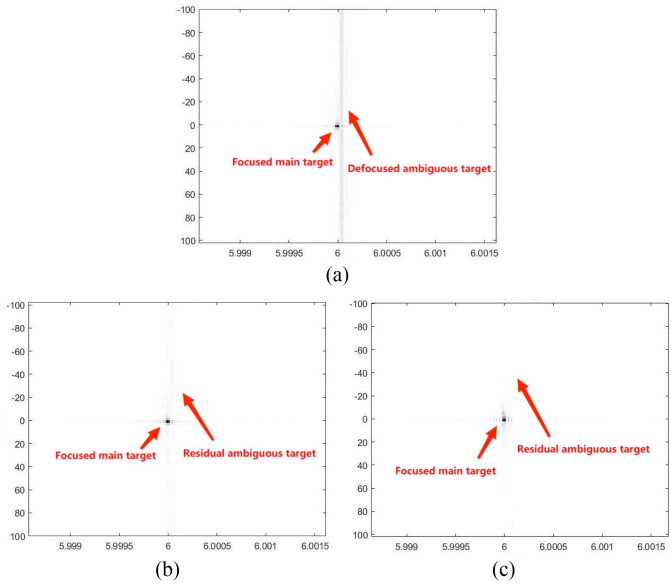

Fig. 3. Imaging results of 0 dB energy difference between the ambiguous and main point targets. (a) Matched filter results. (b) Our method results adopting OMP. (c) Our method results adopting FOCUSS.

method adopting OMP, and by our method adopting FOCUSS, respectively.

In the second case, the energy ratio of the ambiguous target to the main target is 100:1 (ambiguity target energy minus main target energy is 20 dB). According to the above, there is another main target, the slant range of which is $c/(2\mathrm{PRF})$ larger than that of ambiguous target strictly. The reason is to compare the OMP and the FOCUSS algorithms significantly when the main and ambiguous targets are overlapped with each other. Fig. 4 shows the imaging results similar to Fig. 3.

Table V summarizes both the integral and the peak energy ratio of ambiguous target to main target after imaging. It can be seen that although the ambiguous target obtained by the matched filter is defocused, the energy is still very strong and its impact on the main target image is obvious. The method in this article effectively suppresses the ambiguous energy. When the energy ratio is 1:1, the proposed method adopting OMP algorithm suppresses the ambiguous energy by 11.9 dB; the proposed method adopting FOCUSS algorithm, relative to that adopting OMP algorithm, further suppresses the ambiguous energy by 6.9 dB, as shown in Fig. 3. When the energy ratio is 100:1, the proposed method adopting OMP algorithm suppresses the

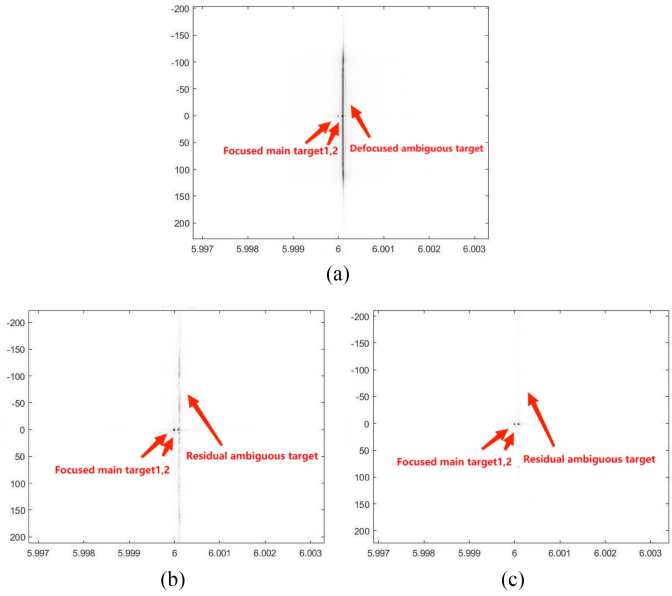

Fig. 4. Imaging results of 20 dB energy difference between the ambiguous and main point targets. (a) Matched filter results. (b) Our method results adopting OMP. (c) Our method results adopting FOCUSS.

TABLE V
ENERGY RATIO OF POINT TARGET BY THREE RANGE AMBIGUITY SUPPRESSION METHODS

Condition of scene	Method	Energy ratio(dB)	
		Integral	Peak
energy difference 0 dB (without noise)	Matched filter	0.0128	−18.9953
	Our method adopting OMP	−11.9414	−26.1393
	Our method adopting FOCUSS	−18.8716	−26.3402
energy difference 20 dB (without noise)	Matched filter	19.3927	1.0088
	Our method adopting OMP	7.9140	−6.1270
	Our method adopting FOCUSS	−6.036	−6.7098
energy difference 0 dB (SNR−30 dB)	Matched filter	0.0175	−8.9656
	Our method adopting OMP	−10.7281	−11.9066
	Our method adopting FOCUSS	−11.2823	−12.1482

ambiguous energy by 11.5 dB, as shown in Fig. 4(b), but the residual ambiguous energy is still serious; the proposed method adopting FOCUSS algorithm further suppresses the ambiguous energy by 13.9 dB, as shown in Fig. 4(c), and the residual ambiguous energy is almost invisible.

In addition, the last three lines in Table V, respectively, show the range ambiguity suppression effect of the proposed method under the condition of adding strong noise. Chosen the energy ratio of ambiguous target to main target is 1:1, the Gaussian white noise is added to the simulated echo, and the signal-to-noise ratio (SNR) is −30 dB. The proposed method adopting OMP suppresses the ambiguity by 10.7 dB, which is comparable with the case without adding noise, and verifies its applicability under noise conditions. The proposed method adopting FOCUSS suppresses the ambiguity by 11.3 dB, the performance of which

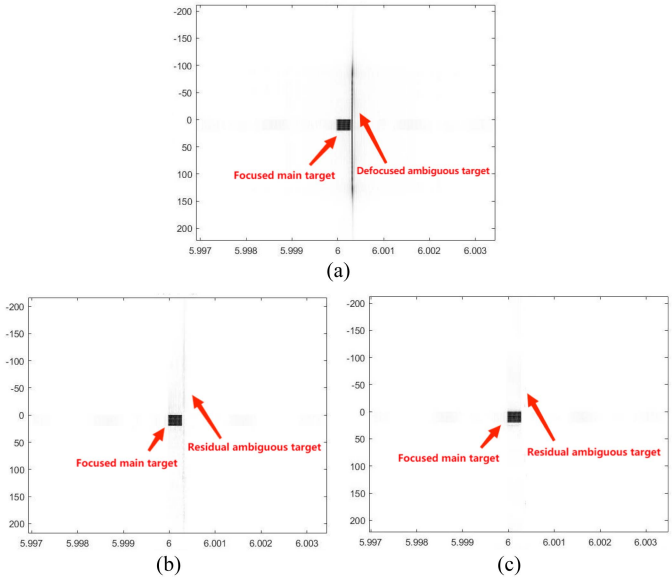

Fig. 5. Imaging results of ambiguous point target and main surface target. (a) Matched filter results. (b) Our method results adopting OMP. (c) Our method results adopting FOCUSS.

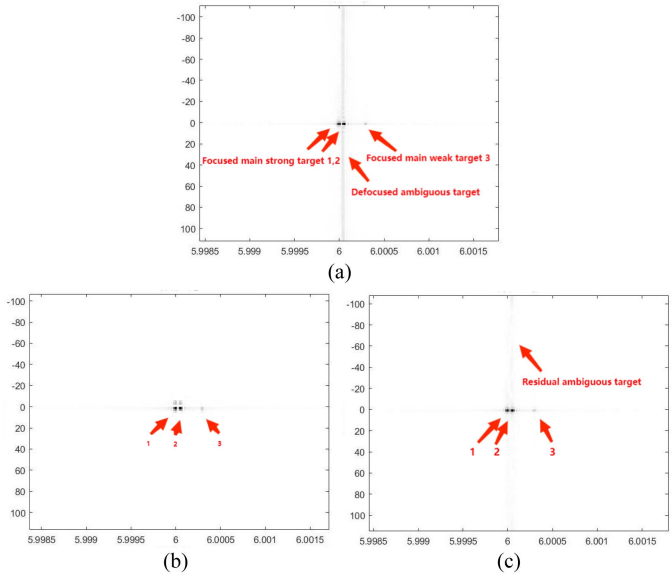

Fig. 6. Imaging results of weak target in main area. (a) Matched filter results. (b) OMP reconstruction only results. (c) Our method results adopting OMP.

TABLE VI
ENERGY RATIO BEFORE AND AFTER RANGE AMBIGUITY SUPPRESSION

Method	Energy ratio(dB)	
	Integral	peak
Matched filter	–0.2622	–1.2186
Our method adopting OMP	–15.1669	–11.8238
Our method adopting FOCUSS	–19.4708	–12.7716

TABLE VII
ENERGY CHANGE OF WEAK TARGET BEFORE AND AFTER IMAGING

Method	Weak target energy (J)	Integral Energy Ratio (dB)
Matched filter	7.2703e+07	–3.4959
OMP only	5.3230e+07	–19.6486
Our method adopting OMP	7.1773e+07	–15.4071

deteriorates quickly due to strong noise. Thus, in the case of strong noise, the superiority of FOCUSS over OMP is no longer obvious.

Then, the simulation is carried out for the surface target in the main imaging area and the point target in the ambiguity area. The energy ratio of the ambiguous point target to the main surface target is 1:1 (ambiguous energy minus main energy is 0 dB). Fig. 5 shows the imaging results obtained by three methods.

Accordingly, Table VI lists the integral energy ratio of the ambiguous point target to the main surface target after imaging. It can be seen that, using the matched filter, the energy of the ambiguous target is equivalent to the energy of the main target, and the impact on the main image is obvious. The method in this article can effectively suppress the ambiguity energy. As shown in Fig. 5(b), compared with the matched filter, the proposed method adopting OMP algorithm suppresses the ambiguous energy by 14.9 dB; as shown in Fig. 5(c), for the proposed method adopting FOCUSS algorithm, relatively to that adopting OMP algorithm, the ambiguous energy is further suppressed by 4.3 dB.

It can be seen that, for the scene where ambiguous energy is equal to main energy, our method adopting OMP algorithm can reduce the energy ratio to below 10 dB. Meanwhile, for the scene where ambiguous energy is 20 dB higher than main energy, it is difficult to achieve fine ambiguity suppression effect for our method adopting OMP algorithm. In this case, fortunately, specific sparse reconstruction algorithms with higher accuracy, such as the FOCUSS algorithm, can still obtain an acceptable suppression effect at the price of efficiency.

Next, we compare the method in this article with the traditional sparse reconstruction method in terms of the detail preservation capability of weak targets, and the simulation is carried out for the point target. Set three point targets from near to far in the main area and one point target in the ambiguity area. The slant range of the second main target is $c/(2\mathrm{PRF})$ larger than that of ambiguous target strictly. The energy ratio of the three main point targets to the ambiguity point target is 25:25:1:25, that is, the third main point target is the weak target. Fig. 6 shows the imaging results obtained by matched filter, by OMP reconstruction only, and by our method adopting OMP, respectively.

Table VII lists the statistical energy change of weak target after imaging and the integral energy ratio of ambiguous target to the sum of three main targets. It can be seen that, by adopting the OMP algorithm only, the range ambiguity is suppressed by 16.2 dB while the weak target energy is also suppressed by 27%. It results in radiation distortion and loss of detail. By using the method in this article, the range ambiguity suppression procedure based on the sparse reconstruction of the ambiguity area has much less impact on the main image. Since the subsequent matched filter algorithm can retain the weak

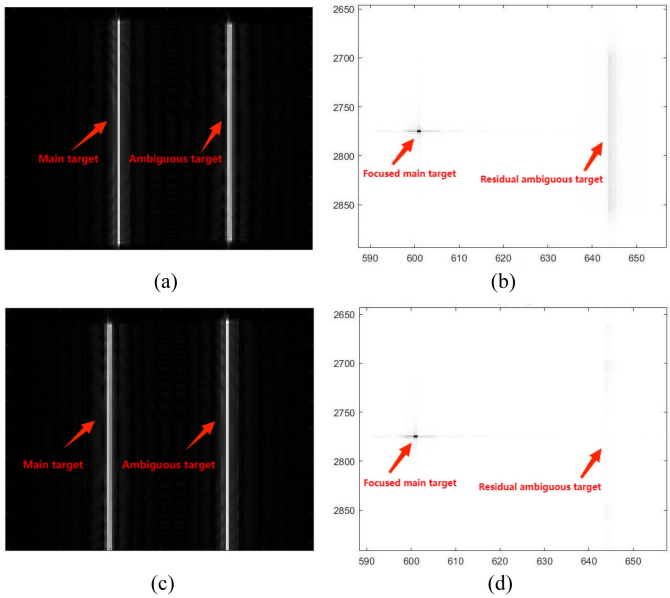

Fig. 7. Imaging results comparison of two ways of range migration correction. (a) Migration correction according to main image. (b) Results according to Fig. 1. (c) Migration correction according to ambiguity image. (d) Results according to Fig. 2.

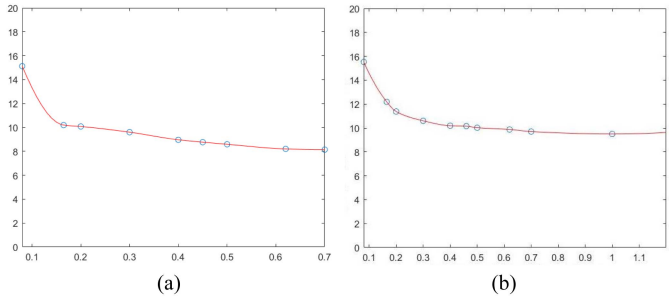

Fig. 8. Ambiguity suppression curve with respect to migration difference. (a) Curve according to Fig. 1. (b) Curve according to Fig. 2.

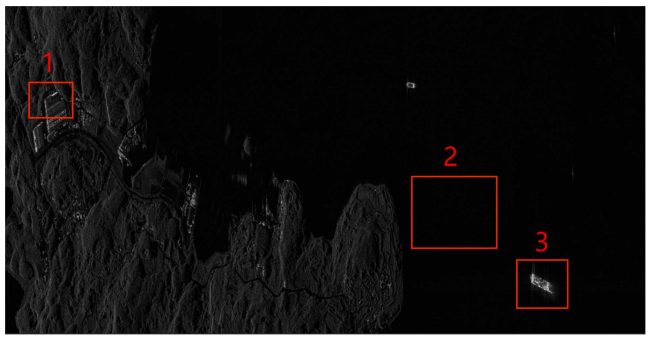

Fig. 9. First actual image of Gaofen-3.

target energy, the weak target energy change does not exceed 2%, and the range ambiguity suppression is 11.9 dB. Therefore, the proposed method has better performance of weak target and detail preservation than OMP-based sparse reconstruction methods.

The following simulation focuses on the validity of the improvement of two-step range migration correction, as shown in Fig. 2. The simulation is carried out for the point target, and the energy ratio of ambiguous point target to main point target is 1:1. In order to facilitate to represent the two-step range migration correction effect on range ambiguity suppression, the synthetic aperture time is adjusted, and thus the migration difference between the main target and the corresponding ambiguous target is changing from less than 0.1 to 1.2 times the range gate.

For instance of migration difference equal to 0.5 range gate, Fig. 7(a) shows the results of range migration correction according to the main image, and the results of range migration correction according to the ambiguity image are shown in Fig. 7(c). The energy ratio amount realized by the ambiguity suppression method in Fig. 1 is 8.767 dB, as shown in Fig. 7(b). The energy ratio amount realized by the ambiguity suppression method in Fig. 2 reaches 10.158 dB, as shown in Fig. 7(d), which is improved by 1.4 dB.

For the one-step range migration correction in Fig. 1, the curve of range ambiguity suppression with respect to migration difference is shown in Fig. 8(a). For the two-step range migration correction in Fig. 2, the curve is shown in Fig. 8(b). The horizontal coordinates are the maximum range migration difference between the main and the ambiguous targets within the synthetic aperture time, and the vertical coordinates are the improvement amount of the energy ratio of ambiguity to main image by the range ambiguity suppression method. The result, as shown in Fig. 8(b), is 2 dB better than those in Fig. 8(a) overall. In Fig. 8(a), the ambiguity suppression performance deteriorates faster, which descends 7 dB as the migration difference grows to 0.7 range gate. Meanwhile, as shown in Fig. 8(b), the performance deteriorates slower, which descends 6 dB as the migration difference grows to 1.2 range gate. Taking the deterioration of 9 dB as the threshold, the tolerance of method in Fig. 1 to migration difference is 0.5 range gate, and the tolerance of method in Fig. 2 is 1.2 range gate.

B. *Simulation of Scene Template of Actual Images*

In this part, we use the actual images of Gaofen-3 [19] satellite as a scene template to simulate and verify the effect of range ambiguity suppression in multiple cases.

The first image is shown in Fig. 9. In the first image, areas 1, 2, and 3 are chosen to form various simulation cases. As shown, area 1 is the Urban area, area 2 is the sea surface, and area 3 is an isolated ship.

Taking area 3 as the main imaging area and area 1 as the ambiguity area, the simulated echo of the main and ambiguity areas is superimposed, and ambiguity image is apparent after matched filtering despite defocusing, as shown in Fig. 10(a). The image by our method adopting OMP algorithm to reconstruction is shown in Fig. 10(b), and that adopting FOCUSS algorithm to reconstruction is shown in Fig. 10(c). It can be seen that the ambiguity suppression effect of our method adopting the OMP is fine. Meanwhile, by replacing the OMP with FOCUSS, better suppression effect can be gained, especially noticeable in the red rectangular window.

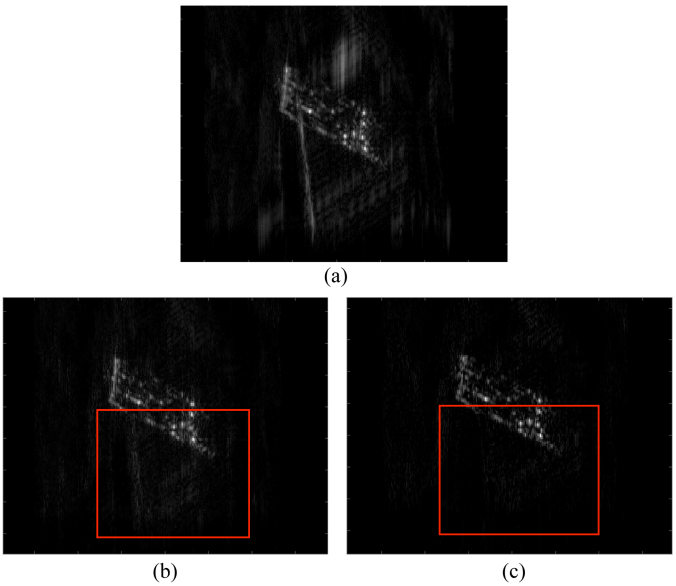

Fig. 10. Imaging results of ship as main image and urban area as ambiguity image. (a) Matched filter results. (b) Our method results adopting OMP. (c) Our method results adopting FOCUSS.

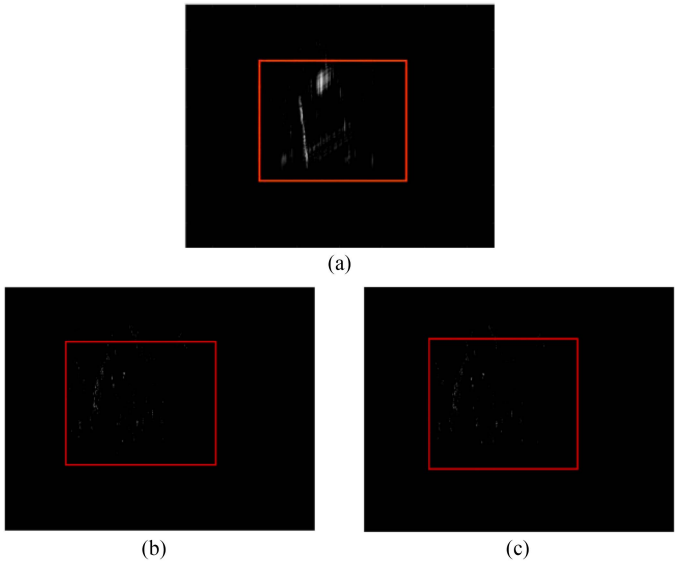

Fig. 12. Imaging results of calm sea as main image and urban area as ambiguity image. (a) Matched filter results. (b) Our method results by reconstructing main and ambiguity areas in terms of (10). (c) Our method results by reconstructing ambiguity area only in terms of (18).

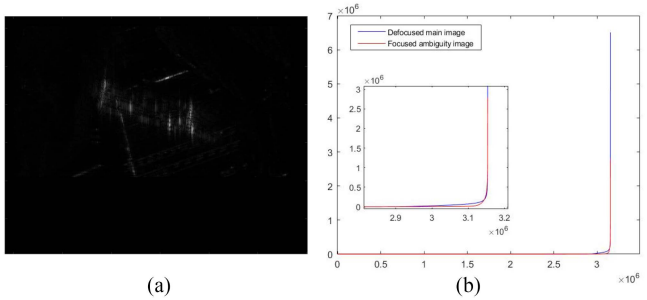

Fig. 11. Amplitude statistics curves of defocused main image (blue line) and focused ambiguity image (red line), sorted according to amplitude value. (a) Image by matched filter of ambiguity area. (b) Amplitude statistics curves.

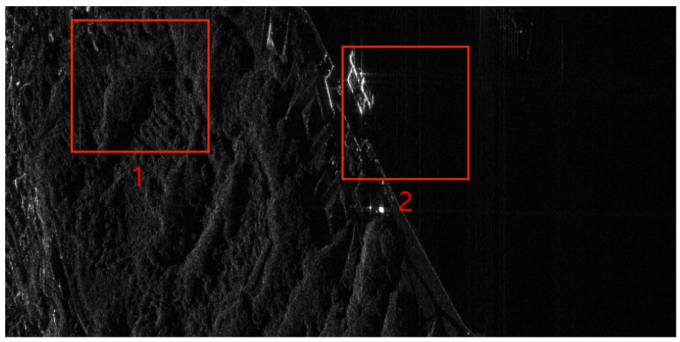

Fig. 13. Second actual image of Gaofen-3.

At this time, the CFAR detection method in [6] cannot be effectively used. Fig. 11(a) shows the image after matched filtering for ambiguity area. As shown in Fig. 11(b), although the main image is defocused, its amplitude statistics is still stronger than that of the ambiguity image. It is difficult to distinguish the main image from the ambiguity image by using CFAR to detect strong points. That is, the CFAR detection method for range ambiguity suppression relies on the up and down chirp modulation system deeply. It is difficult to be extended to the fixed frequency modulation system. However, the method in this article does not depend on the frequency modulation system, which solves the range ambiguity problem in a wider range of circumstances.

Taking area 2 as the main imaging area and area 1 as the ambiguity area, since the range ambiguity suppression is performed for the main area with quite weak energy, i.e., the calm sea surfaces, the simplified sparse reconstruction procedure in (18) instead of that in (10) is used, and it can still obtain good range ambiguity suppression, as shown in Fig. 12. The imaging results of matched filter are shown in Fig. 12(a), and the results of our method by adopting sparse reconstruction in terms of (10) and (18), respectively, are shown in Fig. 12(b) and (c). It can be seen that, if the energy of the main area is quite weak, the sparse reconstruction of our method can be further simplified to reduce the calculation amount.

The second image is shown in Fig. 13. In the second image, areas 1 and 2 are chosen to form another simulation case. As shown, area 1 is the mountainous area, and area 2 is the port area.

Taking area 1 as the main imaging area and area 2 as the ambiguity area, the simulated echo of the ambiguity area is superimposed on that of the main area. As shown in Fig. 14(a), by matched filtering, the defocused port image is appeared superimposed on the focused mountain image. By our method adopting OMP algorithm, there is still some ambiguity energy remaining, as shown in Fig. 14(b), because the ambiguity area is relatively strong. Fortunately, by our method adopting FOCUSS algorithm, the residual ambiguity image is almost invisible, as shown in Fig. 14(c). The FOCUSS algorithm has higher reconstruction accuracy of the ambiguity image than the OMP

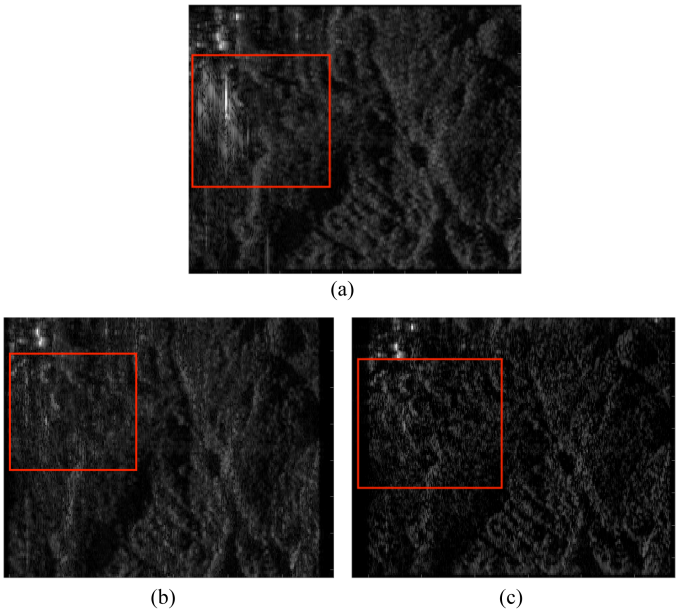

Fig. 14. Imaging results of mountain as main image and port as ambiguity image. (a) Matched filter results. (b) Our method results adopting OMP. (c) Our method results adopting FOCUSS.

algorithm. OMP and FOCUSS algorithms can be selected by considering the requirements of efficiency and accuracy.

IV. Conclusion

In this article, a range ambiguity suppression method combining matched filter and sparse reconstruction is proposed. Compared with the algorithms, which directly use the sparse reconstruction alone to obtain the main image and the ambiguity image, the proposed method only takes sparse reconstruction to the ambiguity areas with strong energy and thus the relatively low sparsity is set for few strong points that needed to be sparsely reconstructed, which could simplify the iterative procedure and reduce the amount of computation. Compared with the algorithms using matched filtering and CFAR to estimate and suppress the range ambiguity, the proposed method significantly expands the applicability due to the independency of the way of frequency modulation and improves the accuracy of range ambiguity suppression due to the combination of the sparse reconstruction algorithm. By adopting the FOCUSS algorithm and performing the improved two-step range migration correction, our method can suppress range ambiguity and preserve details of the main image effectively. It achieves ambiguity suppression of 9 dB when the range migration difference between the main and ambiguous areas is about a single resolution cell. It can obtain ambiguity suppression of 25 dB when the energy ratio of ambiguous to main targets is 20 dB.

References

[1] J. C. Curlander and R. N. Mcdonough, *Synthetic Aperture Radar: Systems and Signal Processing*. New York, NY, USA: Wiley, 1991.

[2] Y. Wang, Z. Ding, P. Xu, K. Chen, T. Zeng, and T. Long, "Strip layering diagram-based optimum continuously varying pulse interval sequence design for extremely high-resolution spaceborne sliding spotlight SAR," *IEEE Trans. Geosci. Remote Sens.*, vol. 59, no. 8, pp. 6751–6770, Aug. 2021.

[3] H. D. Griffiths and P. Mancini, "Ambiguity suppression in sars using adaptive array techniques," in *Proc. IEEE Int. Geosci. Remote Sens. Symp.*, Espoo, Finland, Jun. 1991, pp. 1015–1018.

[4] G. Krieger et al., "CEBRAS: Cross elevation beam range ambiguity suppression for high-resolution wide-swath and MIMO-SAR imaging," in *Proc. IEEE Int. Geosci. Remote Sens. Symp.*, Milan, Italy, Jul. 2015, pp. 196–199.

[5] J. Mittermayer and J. M. Martinez, "Analysis of range ambiguity suppression in SAR by up and down chirp modulation for point and distributed targets," in *Proc. IEEE Int. Geosci. Remote Sens. Symp.*, Toulouse, France, Jul. 2003, pp. 4077–4079.

[6] X. Wen, X. Qiu, B. Han, C. Ding, B. Lei, and Q. Chen, "A range ambiguity suppression processing method for spaceborne SAR with up and down chirp modulation," *Sensors*, vol. 18, no. 5, 2018, Art. no. 1454.

[7] H. Mo and Z. Zeng, "Investigation of multichannel ScanSAR with up and down chirp modulation for range ambiguity suppression," in *Proc. IEEE Int. Geosci. Remote Sens. Symp.*, Beijing, China, Jul. 2016, pp. 1130–1133.

[8] M. Liu, B. Zhang, Z. Xu, Y. Zhang, L. Zhong, and Y. Wu, "Ambiguities suppression for azimuth multichannel SAR based on $L_{2,q}$ regularization with application to Gaofen-3 ultra-fine stripmap mode," *IEEE J. Sel. Topics Appl. Earth Observ. Remote Sens.*, vol. 14, pp. 1532–1544, 2020.

[9] D. L. Donoho, "Compressed sensing," *IEEE Trans. Inf. Theory*, vol. 52, no. 4, pp. 1289–1306, Apr. 2006.

[10] X. Peng, W. Youming, Y. Ze, and L. Chunsheng, "Azimuth ambiguity suppression in SAR images based on compressive sensing recovery algorithm," *J. Radars*, vol. 5, no. 1, pp. 35–41, 2016.

[11] J. Fang, Z. Xu, C. Jiang, B. Zhang, and W. Hong, "SAR range ambiguity suppression via sparse regularization," in *Proc. IEEE Int. Geosci. Remote Sens. Symp.*, Munich, Germany, Jul. 2012, pp. 3811–3814.

[12] J. Tian, L.-H. Kang, X.-L. Sun, Z. Li, and B.-C. Zhang, "Experiment based on orbit satellite and application for sparse microwave imaging," *J. Commun.*, vol. 38, no. Z2, pp. 37–42, 2017.

[13] H. Bi, B. Zhang, W. Hong, and Y. Wu, "Verification of complex image based sparse SAR imaging method on Gaofen-3 dataset," *J. Radars*, vol. 9, no. 1, pp. 123–130, 2020.

[14] Z. Xu, M. Liu, G. Zhou, Z. Wei, B. Zhang, and Y. Wu, "An accurate sparse SAR imaging method for enhancing region-based features via nonconvex and TV regularization," *IEEE J. Sel. Topics Appl. Earth Observ. Remote Sens.*, vol. 14, pp. 350–363, 2020.

[15] H. Bi, B. Zhang, X. X. Zhu, W. Hong, J. Sun, and Y. Wu, "L1-regularization-based SAR imaging and CFAR detection via complex approximated message passing," *IEEE Trans. Geosci. Remote Sens.*, vol. 55, no. 6, pp. 3426–3440, Jun. 2017.

[16] R. Chartrand, "Exact reconstruction of sparse signals via nonconvex minimization," *IEEE Signal Process. Lett.*, vol. 14, no. 10, pp. 707–710, Oct. 2007.

[17] A. Chatterjee and P. W. T. Yuen, "Rapid estimation of orthogonal matching pursuit representation," in *Proc. IEEE Int. Geosci. Remote Sens. Symp.*, 2020, pp. 1315–1318.

[18] Z. Xu, H. Zhang, Y. Wang, X. Chang, and Y. Liang, "L 1/2 regularization," *Sci. China Inf. Sci.*, vol. 53, pp. 1159–1169, 2010.

[19] B. Han et al., "The GF-3 SAR data processor," *Sensors*, vol. 18, no. 3, 2018, Art. no. 835.

Meng Qi received the bachelor's degree in electronic engineering from the Beijing Institute of Technology, Beijing, China, in 2019, and the M.S. degree in signal and information processing from the University of Chinese Academy of Sciences, Beijing, China, in 2022.

She is currently with the Aerospace Information Research Institute of QiLu, Chinese Academy of Sciences, Jinan, China. Her research interest includes radar signal processing and compressed sensing.

Lijia Huang received the B.S. degree in electronic engineering from Beihang University, Beijing, China, in 2006, and the Ph.D. degree in signal and information processing from the Graduate University of Chinese Academy of Sciences, Beijing, China, in 2011.

Since 2011, she has been with Aerospace Information Research Institute, Chinese Academy of Sciences, Beijing, China. Her current research interests include the spaceborne SAR signal processing and image interpretation.

Xiaochen Wang received the B.S. and M.S. degrees in surveying and mapping form the China University of Petroleum (East China), Qingdao, China, in 2013 and 2016, respectively, and the Ph.D. degree in signal and information processing from the Institute of Remote Sensing and Digital Earth, Chinese Academy of Sciences, Beijing, China, in 2019.

His research interests include SAR imaging mechanism over ocean waves.

Jie Li received the bachelor's degree in signal and information processing from the Beijing Institute of Technology, Beijing, China, in 2019. She is currently working toward the Ph.D. degree in signal and information processing with the University of Chinese Academy of Sciences, Beijing, China.

Her research interests include TomoSAR imaging and deep learning.

Bingchen Zhang received the bachelor's degree from the University of Science and Technology of China, Hefei, China, in 1996, and the M.S. degree from the Institute of Electronics, Chinese Academy of Sciences (IECAS), Beijing, China, in 1999, both in signal and information processing.

Since 1999, he has been a Scientist with IECAS. His research interests include synthetic aperture radar (SAR) signal processing and airborne SAR system design, implementation, and data processing.